Instabilities in a dusty plasma with ion drag and ionization

D. Samsonov* and J. Goree*,†
Max Plank Institut für Extraterrestrische Physik, Giessenbachstrasse, 85740, Garching, Germany
(Received 13 March 1998)

Low-frequency modes that develop as a result of an instability in a dusty rf discharge plasma were studied experimentally, leading to an empirical explanation for the instability. In the experiment, particle diameter grew with time. Two instability modes appeared after growth to a sufficient size. A filamentary mode appeared abruptly, and later a great void mode developed as a dust-free region with an intense glow inside and a sharp boundary outside. These modes were characterized by two-dimensional laser light scattering, video imaging, optical emission spectroscopy, Langmuir probe measurements, and Fourier analysis of the fluctuation spectrum. Dust growth was measured by electron microscopy and optical extinction, yielding the dust particle size and dust number density. The electron density was found to be enhanced inside the great void, due to an absence of electron depletion on the dust grains. The great void was explained by the ion drag force, which becomes stronger than the opposing Coulomb force once the particle size reaches a critical diameter. When a dust-free region develops, its electron density is enhanced, the ionization rate increases, and the ion flow that pushes particles outward is further augmented. The plasma used in the experiment grew particles by sputtering of the electrodes, although the same instabilities are expected to occur in other types of dusty plasma discharges as well. [S1063-651X(99)00801-6]

PACS number(s): 52.35.−g, 52.80.−s, 52.25.Vy

I. INTRODUCTION

A dusty plasma is an ionized gas containing small particles of solid matter, which either grow in the plasma or are introduced externally. The particles acquire a large electric charge by collecting electrons and ions from the plasma. Interest in dusty plasmas arises from several scientific disciplines and industrial applications, including contamination of materials during plasma processing, nanoparticle manufacturing, astrophysics, and basic science.

In semiconductor manufacturing, particle contamination can significantly decrease the yield of semiconductor devices and thus increase production costs. Clouds of particles have been found in plasmas for silicon etching [1], chemical vapor deposition [2,3], and sputter deposition [4,5]. It appears that particle production and trapping is ubiquitous to all rf discharges [6]. Particles trapped in a plasma can fall to a silicon wafer and contaminate it.

For producing special materials, small particles formed in a plasma can have desirable properties, such as a small monodispersive size. Ceramics have been fabricated from particles synthesized in a pulsed rf discharge [7]. Nanocrystalline powders of pure metals, binary alloys, intermetallics, and ceramics have been produced by magnetron sputtering [8]. Phase separated materials, which are used in electronic, magnetic, and glass-ceramic applications, can also be synthesized, as has been demonstrated by making molybdenum nanoparticles embedded in aluminum [9].

Dusty plasmas are of great interest in astrophysics because of the ubiquitous presence of dust particles in interstellar [10] and interplanetary space [11], planetary rings [12], comet tails, protoplanetary disks, and moon and asteroid surfaces [13]. In addition to numerous theoretical and observational works, there have been experimental attempts to synthesize cosmic dust in the laboratory [14,15].

In the field of basic plasma physics, dusty plasma research topics have included charging [16], waves and instabilities [17–21], and Coulomb crystallization [22–27]. The latter is sometimes referred to as the formation of a ''plasma crystal,'' which has been shown to exhibit phase transitions [28–30] and compressional waves [31], among other phenomena.

In this paper we report a series of experiments to characterize an instability in a dusty plasma that was reported previously by Praburam and Goree [32]. In that experiment, low-frequency modes were tentatively identified as having properties of either an ionization wave or a compressional dust acoustic wave. As the particle size grows, the instability develops in two stages: first a ''filamentary mode'' of approximately 100 Hz in which the ionization rate and dust number density are both modulated, and then a ''great void mode'' which is similar, except that there is a single prominent void in the dust cloud which rotates azimuthally with a frequency of about 2 Hz. The filamentary mode appears suddenly when the dust grain diameter exceeds a certain critical value. We use an rf sputtering discharge, although the same instability is likely to occur in many types of dusty plasmas formed in a gas discharge.

We used many more diagnostics and measurements than in Praburam and Goree's experiment, and these allow us to make much more definitive conclusions. Among the results reported below, we found that the instability develops when the particle diameter reaches a critical size. Rarefactions in the dust number density coincide exactly with an enhanced glow, where there is presumably a locally increased ionization rate that produces an outward ion flow.

These and other results lead us to an empirical explana-

*Permanent address: Department of Physics and Astronomy, The University of Iowa, Iowa City, IA 52242.
†Author to whom correspondence should be addressed. Electronic address: john-goree@uiowa.edu

tion of the instability: when the particle size is large enough, ion drag pushes particles away from a region of locally enhanced ionization with enough force to overcome an opposing Coulomb force. As the particles are pushed away from the ionization hot spot, they no longer deplete electrons there, and this allows the rate of electron-impact ionization to grow even more intense.

Thus we propose that the modes are a type of ionization instability unique to dusty plasmas in a gas discharge. The modes inherently involve ion drag, which applies a far stronger force on charged dust particles than on ions or electrons, due to the high charge of the dust. Nor is it likely that they can be seen in a dusty plasma that is not sustained by internal ionization. The class of plasmas where this mode is likely to be seen includes, for example, plasma processing discharges and plasma crystal experiments, which both involve a particle cloud immersed in a gas discharge.

II. PREVIOUS WORK

A. Dust growth

Laboratory dusty plasmas can be prepared either by using premanufactured particulates or by growing them in the plasma itself, by condensing gases into solid particles. Particles grown in the gas phase become larger with time due to three processes [33]: (i) formation of clusters (nucleation), (ii) formation of aggregates by coagulation, and (iii) growth by deposition, i.e., accretion of individual ions and neutral species from the gas. For small particles, coagulation can represent the fastest of the growth mechanisms [33]. This is possible when the diameter and therefore the charge is small. For extremely small particles, the charge sometimes fluctuates to zero or even positive values, which favors coagulation [16,34]. For larger particles, the charge is greater and coagulation is inhibited by Coulomb repulsion. In that case, deposition of individual ions or neutral species from the gas phase is the primary growth mechanism.

B. Instabilities in dusty plasmas

Low-frequency modes observed experimentally by Praburam and Goree [32] were tentatively identified as having properties of either an ionization wave or a compressional dust acoustic wave. The experiment was performed in a parallel-plate rf discharge, which grew dust particles by sputtering graphite electrodes. Two modes were identified: the filamentary mode and the great void mode. Both modes had low frequency, on the order of 10 Hz. Praburam and Goree reported visual observations that the glow was modulated during the great void mode, suggesting that ionization is disturbed in the mode, although no precise measurements were made to relate the movement of the dust and the glow. In this paper we report experiments similar to those of Ref. [32], but with diagnostics and measurements to characterize the modes in far greater detail.

In addition to modifying the properties of existing wave modes, such as ion acoustic or electron cyclotron modes, as shown in Refs. [35] and [36], the presence of dust in a plasma gives rise to a dust acoustic mode, which was predicted theoretically in Ref. [37] and others [38–41]. Dust acoustic waves were observed experimentally in a Q machine by Barkan and co-workers [17,19] and in a dc glow discharge by Thompson *et al.* [42]. Dust acoustic waves in the strongly coupled regime were studied by Pieper and Goree [31].

The dusty plasma literature to date includes little work on ionization instabilities. Theories of ionization instabilities in a dusty plasma were presented in Refs. [43] and [44]. The fluid model of Ref. [43] predicts that an ionization instability spontaneously excites dust-ion-acoustic and dust acoustic waves. The instability arises because ionization is faster in the wave crests than in the wave troughs, due to the rapid increase in the ionization cross section with electron energy. D'Angelo [44] contended that Shukla and Merfill's equations included an inappropriate ionization term and neglected loss mechanisms, and as a result the predicted dispersion relation does not include the energy dependence of the ionization cross. D'Angelo developed a dispersion relation that yields a negative growth rate for the dust acoustic wave. The only unstable mode was the much higher frequency ion acoustic wave. Stabilizing factors include neutral drag on dust, ion-neutral collisions, and ion viscosity, which are all dissipative processes. One factor not included in D'Angelo's model is ion drag, i.e., momentum transferred to charged dust particles by Coulomb collisions with flowing ions. We propose in this paper that ion drag is the destabilizing mechanism that accounts for the modes we observe. After we submitted this paper, D'Angelo reported a modified theory which does include an ion drag force, leading to an instability [45].

C. Ionization instability in dust-free plasmas

Ionization waves and instabilities, i.e., striations, in dust-free plasmas have been studied for decades. The basic types, as summarized by Garscadden [46], include standing striations, moving striations, and relaxation oscillations. The latter are dependent on external circuits and plasma boundaries. Ionization waves in general are known to occur in rare, molecular, and electronegative gases. Ionization instabilities in electronegative gases arise due to negative ions, which are in some respect similar to negatively charged dust particles and can cause the same effects, like electron depletion and alteration of electron temperature. According to Ref. [47] an instability can develop if the dissociative attachment rate increases strongly with the electric field. The opposite process, associative detachment, can also cause an instability in a plasma with negative ions [48].

III. EXPERIMENTAL PROCEDURE

A. Experimental setup

The plasma discharge apparatus shown in Fig. 1 was similar to that of Ref. [32]. A radio-frequency capacitively coupled discharge was formed between two parallel-plate electrodes. The electrodes were 8 cm in diameter and separated by 2 cm, and both were water cooled. They were covered with graphite targets, which were sputtered by ions during the experiment. The resulting carbon vapor condensed in the gas phase, producing nanometer size particles. The upper electrode was powered by a radio-frequency generator, while the lower was grounded. The generator was coupled to the electrode through an impedance matching network and a

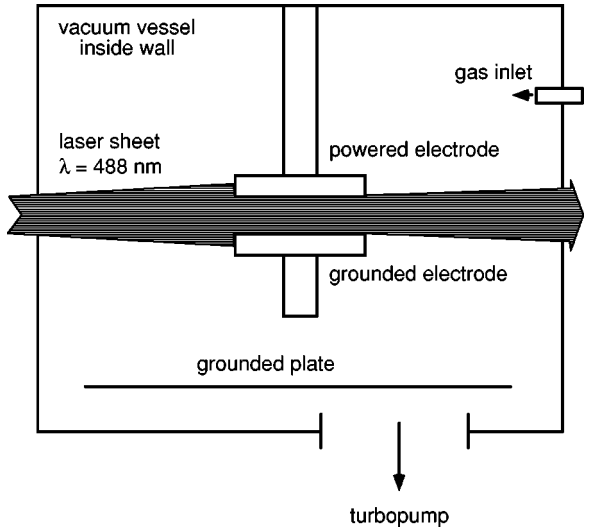

FIG. 1. Sketch of the experimental setup, side view. A sheet of laser light illuminates dust particles.

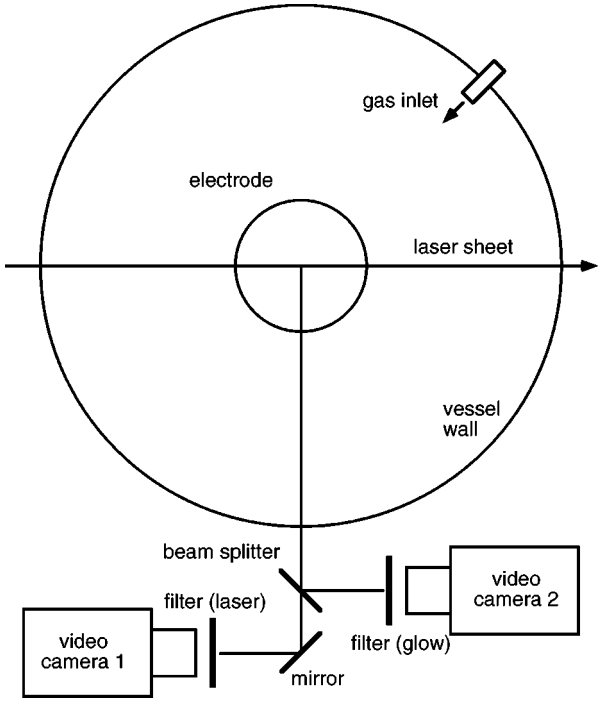

FIG. 2. Experimental setup, top view. Two video cameras, fitted with spectral line filters, view the same interelectrode region through a beam splitter.

coupling capacitor. A power of 100 W was applied, developing a dc self-bias of -300 V. Only electrons can respond to the rf frequency of 13.56 MHz. Ions and dust particles are able to move only in response to dc or low-frequency fields. The electron temperature in a dust-free plasma was $T_e = 3$ eV, as measured by the Langmuir probe described later. Argon pressure was maintained at 400 mtorr. For most of our experimental runs, we flowed gas at 60 sccm, although we also carried out tests without gas flow. For the experiments reported here, the vacuum base pressure was below 10^{-6} torr. At higher base pressures, particles did not grow in the gas phase, suggesting that impurity gas species such as nitrogen, oxygen, and water vapor can inhibit particle formation.

B. Electron microscopy

To measure the growth of the particle size, the discharge was interrupted at different times in a repeated series of experiments. Some of the dust particles fell to the lower electrode, which we removed from the chamber. We then installed it, with the particles intact, in a Hitachi S-4000 field emission scanning electron microscope (SEM). Surface melting by the electron beam was avoided by minimizing the specimen exposure to the beam. Particle diameters were measured directly on the micrographs by a caliper. Fifteen measurements were taken per micrograph, and then the average and standard deviation were calculated. Size measurement errors were due to diffuse boundaries of carbon particles, deviations from both spherical shape and average size.

C. Optical extinction

To find the dust number density, it was not possible to rely on the SEM images, since only a fraction of the particles fell to the lower electrode. Instead we measured the number density *in situ*, by extinction of a laser beam. After passing through the dust cloud, the beam struck a matte surface to reduce the intensity, and scattered light was collected with a photomultiplier tube (PMT). This signal was recorded for the whole duration of the dust growth cycle using a digital oscilloscope. By smoothing the data and subtracting the average intensity in the absence of dust, we obtained the optical extinction. Then using the code from Ref. [49], which is based on Mie scattering theory [50,49], we calculated the dust number density. Input parameters in this calculation were the particle diameters from SEM measurements interpolated by a fourth-order polynomial and a refractive index of $(1.95-0.66i)$ based on Ref. [51]. The particle cloud was detected after about 10 s after the discharge was started when the particles were smaller than 50 nm. However, the smallest diameter of the particles measured by SEM, which was 50 nm (taken at 15 s), is the smallest particle diameter for which we can reliably calculate the number density.

The error we report for the number density is based only on the uncertainty in the particle diameter. Additional systematic errors might be created by the value of the refractive index and the applicability of the Mie scattering theory. To assess the error that might be introduced by the refractive index, it is useful to consider that measurements by experimenters using 6 μm diameter carbon particles [52] yielded a refractive index of 1.7 and an extinction coefficient of 0.8, which are somewhat different from the values we assumed.

D. Video imaging

The video setup shown in Fig. 2 provided synchronized images from two video cameras viewing the same subject area. One camera was always used to image a spectral line of the glow. This is sometimes called spatially-resolved optical emission spectroscopy [53,54]. The other camera was used either to image a second spectral line, or to image the dust by laser light scattering (LLS). An optical bandpass filter was installed in the camera, between the lens and the CCD, to admit the desired spectral line.

So that the two cameras viewed exactly the same sampling volume, we aligned them through a cube beamsplitter and a mirror. Video was recorded on two SVHS VCRs using a synchronized time code so that images from individual video frames could be compared at exactly the same time from the two cameras. Frames were digitized at a 640×480 resolution with an eight-bit monochrome frame grabber.

The spectral lines of the glow are the result of electron-impact excitation of argon neutral atoms [55]. An increased glow is generally an indication of electrons that are either more dense or more energetic. One camera was always used to detect the Ar I 763.5-nm line, produced by the decay of the $4s[3/2]^\circ - 4p[1/2]$ transition at 13.17 eV. When the second camera was used for the glow (for the purpose of imaging the electron temperature as explained below) it was fitted with a filter for the Ar I 549.6-nm line, produced by the $4p[5/2]-6d[7/2]$ transition at 15.33 eV.

To illuminate the dust cloud for LLS imaging, a sheet of laser light was formed by passing a 488 nm argon-ion laser beam through a cylindrical lens. The laser was operated at less than 1 W of power. The laser sheet was oriented in a vertical plane for some images and a horizontal plane for others.

In addition to the video measurements of LLS, we also recorded a LLS signal from a single point in the discharge, using a PMT. This allowed us to produce a time series of the LLS intensity from a single point more conveniently and at a higher digitizing rate than from the video. In this setup, a lens was focused on a region <1 cm in diameter, located on the midplane between the electrodes, approximately halfway between the central axis to the electrode edge. A digitized time series of 50 000 samples at 100 samples per second was processed by applying multiple Fourier transformations, each with a Hann window 1024 samples wide, which was shifted along the time coordinate. This procedure yielded the spectral power as a function of time and frequency.

E. Electron temperature imaging

We used the line ratio method of measuring the electron temperature, using separate images of two spectral lines of the optical glow. Since the glow is the result of electron-impact excitation, the ratio of intensities of two spectral lines indicates the relative population of electrons in the distribution function at the two excitation energies. If the electron distribution is Maxwellian, this yields the electron temperature. If not, it indicates an effective temperature, in the energy range of the excited states. The latter is often the case for a low-pressure gas discharge, such as ours, where the excited states have an energy greater than the electron temperature.

A measurement of the electron temperature can be made if a specific atomic physics model is used. The corona model is valid for a low density plasma [56,57]. It assumes an optically thin plasma, a Maxwellian electron distribution function, a low population of the excited states, excitation by electron impact, and deexcitation by radiative decay. The model does not include the processes of stepwise excitation (via metastable states), or by cascades from upper levels, nor does it include quenching by collisions with neutral atoms. The intensity ratio of two spectral lines for a neutral atom was then given by Rhoades and Gorbatkin [58],

$$I_1/I_2 = CT_e^{-0.75}\exp[(E_2-E_1)/T_e], \tag{1}$$

where E_1 and E_2 are the excitation energies for the lower and upper levels respectively, and T_e is the electron temperature in eV. The constant C can be evaluated from comparison to measurements by other methods, or it can be calculated from the atomic physics as in Ref. [59]. Alternatively the line ratio can be calculated by models which are free from restricting assumptions of corona model as in Refs. [60,61], but which require knowledge of the excitation cross sections for many atomic transitions.

To interpret our intensity ratio images, we shall use the fact that in Eq. (1) the intensity ratio I_1/I_2 decreases monotonically with T_e. We do not quantify the temperature, since we did not evaluate the constant C. Our line ratio images will prove to be useful in determining whether an enhanced glow in a certain region of the discharge is due to electrons that are hotter, or simply denser than elsewhere in the plasma.

We imaged the discharge in two spectral lines, using the two video cameras shown in Fig. 2. The two video signals were recorded synchronously using the two VCRs with a common time code. Digitizing the frames, and taking into account the spectral sensitivities of the CCD and the bandpass filters, we computed the line ratio of each pixel in the image. In this way, we produced line-ratio images of the discharge.

F. Langmuir probe measurements

A Langmuir probe was used to measure the floating potential and electron temperature of the discharge. The probe design was made according to the recommendations in Refs. [62,63] to avoid common sources of errors in probe measurements, including contamination of the probe tip and insulator, too large a probe size, rf distortion, and low-frequency noise and drift. The probe had a rf compensation reference electrode connected to the probe tip by an internal shunt capacitor. It also had internal choke inductors to suppress rf current at 13, 26, and 40 MHz.

IV. EXPERIMENTAL RESULTS

A. Particle growth

The particles grew in diameter as a function of time. This is a crucial feature of the experiment, because we will later show that the development of the instabilities depends critically on the particle diameter.

The shape of the particles was roughly spherical, and they were monodisperse, as shown in Fig. 3. For spherical particles, the charge is proportional to the particle radius [16]. Thus the charge on a particle also grew as a function of time in the experiment.

Time series for the particle size and number density are shown in Fig. 4. The dust number density was calculated using Mie code from Ref. [49] directly from the optical extinction time series which was smoothed to reduce noise. The dashed lines indicate the error due to the particle diameter uncertainty.

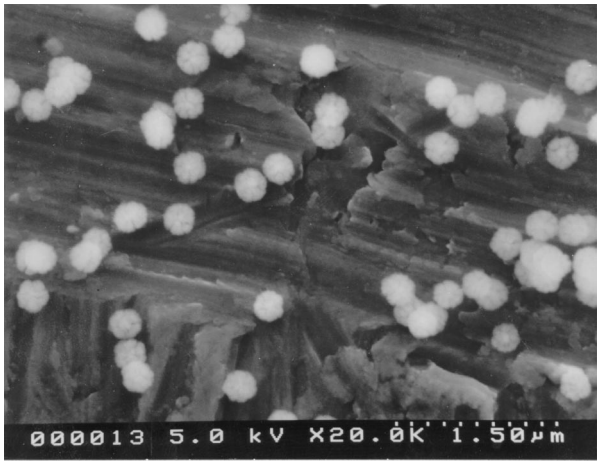

FIG. 3. Electron micrograph of dust particles collected on the lower electrode after 6 min of dust growth. The raspberrylike appearance may be due to growth by coagulation of smaller particles. The calibration bar (a series of 11 tick marks) of length 1.5 μm indicates the size.

When the discharge was first turned on, there was no dust. A particle cloud became detectable by optical extinction about 10 s after the discharge started (presumably particle growth began before then, at a size too small for us to detect). Thereafter, the particles grew larger in size and fewer in number. During the first 40 s the particle diameter grew fast while the number density decreased rapidly. Then the growth slowed down while the number density remained a constant until about 150 s, when a more rapid growth resumed. Our growth shown in Fig. 4 is similar to the growth observed by Boufendi in a silane discharge (Fig. 4 in Ref. [33]) except that the time scale in the silane discharge is more rapid. We assume that the same three-stage growth mechanism takes place in our case: nucleation, coagulation, and accretion. Fast particle growth and the number density decrease at later time in our experiment is probably due to the instability.

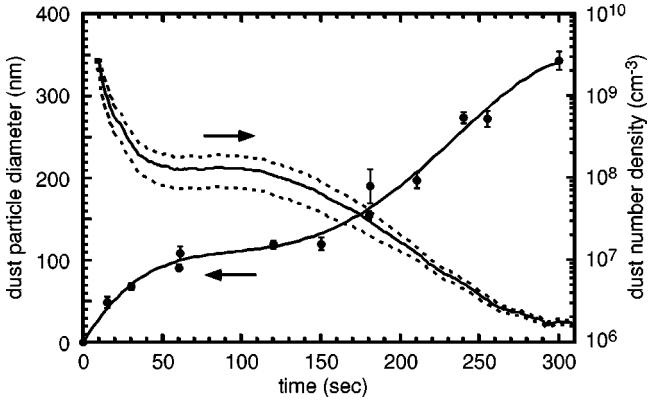

FIG. 4. Dust number density from optical extinction and dust particle size from electron micrographs. The smooth curve through the size data points is a fourth-order polynomial fit, which was used in computing the number density. The dashed lines indicate the number density error based on the uncertainty in the particle diameter.

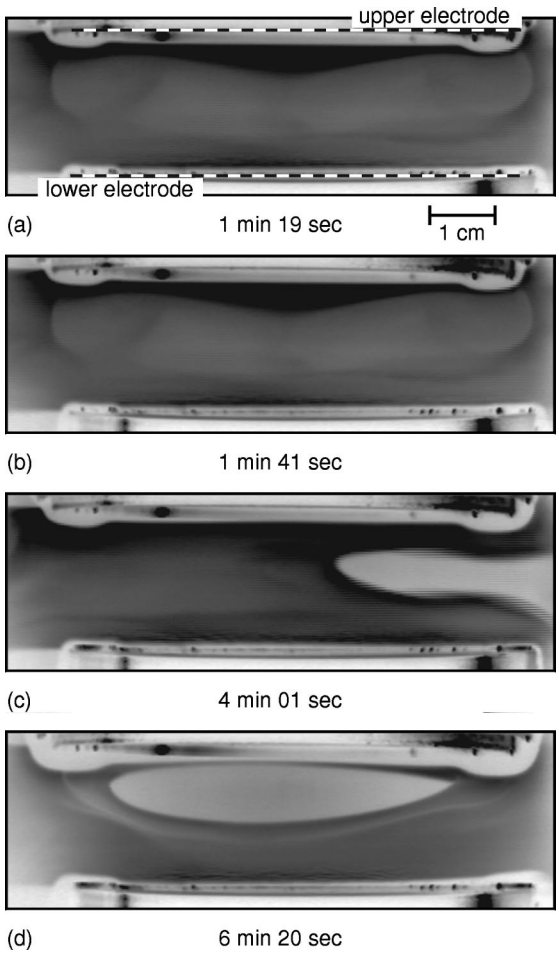

FIG. 5. Images of LLS from the dust, side view. A vertical sheet illuminated the dust. Darker grays correspond to more dust. (a) No instability. (b) Filamentary mode. The filaments can be seen only in Fig. 6(b) or in a moving video, which can be seen on an internet server (Ref. [64]). (c) Great void mode. (d) Instability stops.

B. Instability cycle

The instability was part of a cycle that repeated itself over and over. At first the dust cloud began growing, and it was stable. Later, as the dust grains grew in size, the filamentary mode appeared abruptly. This underwent a transition to the great void mode, which grew until the void, or hole in the dust cloud, grew to fill the entire discharge, and the instability stopped. This marked the end of one cycle. A new cycle then started, with a stable cloud forming in the pristine plasma that had filled most of the interelectrode volume. The rest of the sequence repeated, beginning with the filamentary mode.

C. Initial stability

In the initial stable stage, the dust cloud and the discharge glow were homogeneous. Images are shown in Fig. 5(a) for the LLS, and in Fig. 6(a) for the optical glow. The absence of an instability can be seen in the smooth curve for $t<160$ s in Fig. 7. During this initial stable stage, the particles grew in size and diminished in number density. The floating potential in the fresh plasma began at approximately 9 V, when the dust was just beginning to grow, and it declined during the first 50 s as the dust depleted more and more electrons.

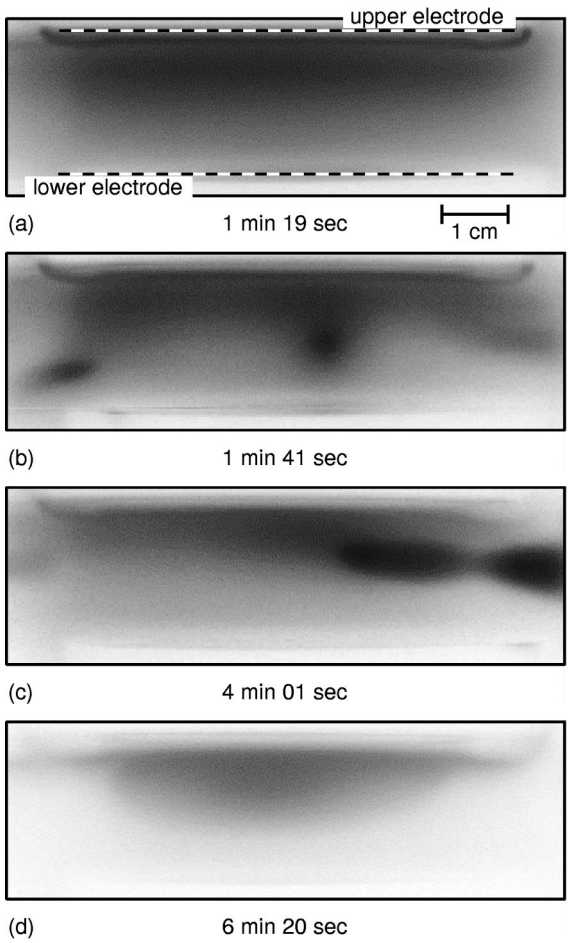

FIG. 6. Optical emission from the discharge, side view. Darker grays correspond to more glow. These images were recorded simultaneously with those of Fig. 5. Images appear more diffuse for the glow, compared to LLS, because they are images of a volume rather than a sharp cross section. (a) No instability. (b) Filamentary mode. Three dark spots left, center, and right are the filaments. (c) Great void mode. (d) Instability stops.

D. Filamentary mode

The filamentary mode instability appeared, with a sudden onset, 75 s after the discharge was turned on. As can be seen in Fig. 7, this mode appeared faster than the 100 s^{-1} digitizing rate of our PMT detector. Apparently the instability grew to a nonlinear saturated level in less than 10 ms.

The filaments were beamlike striations in the dust density and glow. The beams pointed primarily in the radial direction. These are not obvious in the still LLS image of Fig. 5(b) due to a small fractional variation of the dust number density. Three filaments, of size up to 1 cm, can be seen as dark spots in the discharge glow of Fig. 6(b). The filaments are more conspicuous in a moving video (which can be downloaded from Ref. [64]), where they appear as a flickering in both the LLS and glow.

It is useful to remember that the glow serves as an indicator of the same energetic electrons that cause electron-impact ionization. The fact that the glow is modulated suggests that we are observing a type of ionization wave or striation. Similarly, the fact that the dust density is modulated is an indication that electric fields are present at sufficiently low frequency that they move the dust particles about.

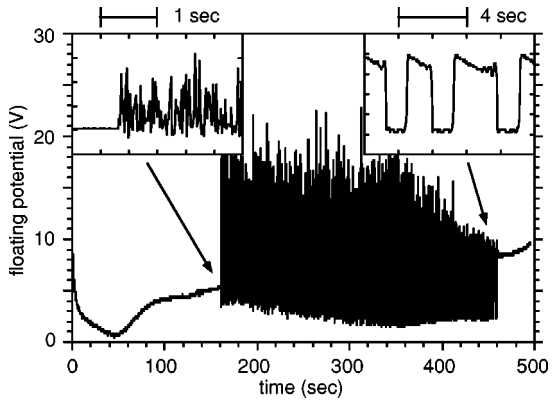

FIG. 7. Floating potential of a Langmuir probe vs time. The sudden onset of the filamentary mode is shown in the left inset. The variation of the potential as the great void passes the probe is shown on the right inset. The data here and in Fig. 8 were taken in a discharge with a longer instability cycle than for all other figures.

The synchronized videos revealed that the regions of brighter glow coincided with a lower dust density. This critical result will be seen again in the great void, and offers a significant clue in explaining the instabilities.

The spectrum of the filamentary mode is broadband, with a peak at about 100 Hz. This is revealed in the spectrum of the floating potential fluctuations, shown in Fig. 8. The frequency of these fluctuations is below the dust plasma frequency, which is estimated in Sec. IV E. We were unable to characterize the motion and velocity of the striations in the filamentary mode because the fluctuation frequency was too high to be tracked using 30 frames-per-second video cameras, or with the human eye for that matter. What we can say is that the modes were not stationary, because we did see them flicker. The great void mode, which we discuss below, was slower and therefore easier to characterize. For this reason, we will present more data on the great void mode than on the filamentary mode.

The physics conclusions from our observations of the filamentary mode, which we will use later in developing a phenomenological model of the instability, include the following: (1) The particle size or charge is a critical parameter for the onset of the instability. (2) The mode is a type of ionization wave or striation. (3) Dust is moved about in the wave,

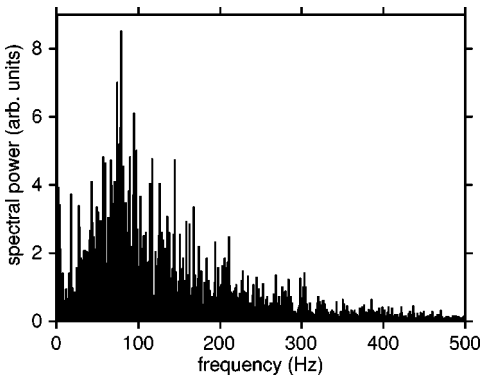

FIG. 8. Spectral power of the floating potential during the filamentary mode, for the same conditions as Fig. 7.

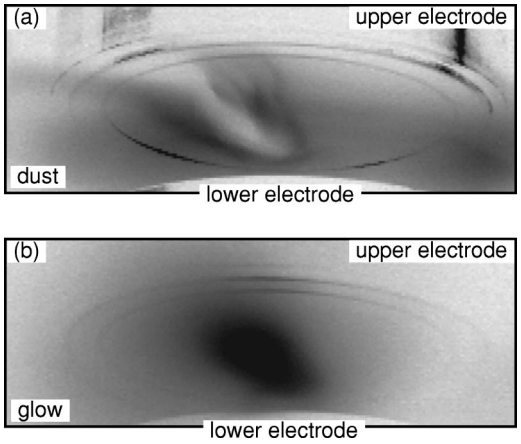

FIG. 9. View of the great void mode. Video cameras viewing upward at oblique angle produced images of LLS from the dust (a) and optical emission (b). Dust is illuminated with a horizontal laser sheet. The enhanced glow inside the great void indicates an enhanced ionization rate. The void in the dust coincides with the enhanced glow.

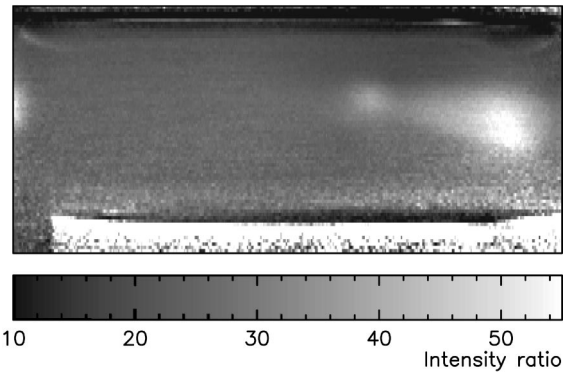

FIG. 10. Line ratio image during the great void mode. The gray scale corresponds to the ratio of the spectral intensities of the spectral line at 763.5 nm to that at 549.5 nm. Darker grays correspond to hotter electrons in the energetic tail of the distribution. The lower electrode appears as a white band at the bottom. Electrons appear to be cooler in the void, despite the enhanced glow, indicating that the enhanced glow must be due to denser electrons. The image shown is $2.5\times5.7\ \mathrm{cm}^2$.

and the mode has a correspondingly low frequency. (4) Ionization is enhanced when the dust number density is diminished.

E. Great void mode

As the dust continued to grow in diameter, a void in the dust appeared 2.5 min after the start of the discharge. The void can be seen in panel (c) of both Figs. 5 and 6, and in the oblique horizontal view shown in Fig. 9. As in the radial filaments in the filamentary mode, the region of reduced dust density coincided with a brighter discharge glow.

What distinguishes the filaments from the great void, leading us to designate them separately, are the following differences. Only a single large void appears, versus more numerous and smaller radial spokes in the filamentary mode. (It is the singularity and size of the void that leads us to call it the ''great void.'') The great void moves more slowly than the filaments. The rarefaction of the dust number density is extreme in the case of the great void: it is 100% dust free. Unlike the filaments, the void does not appear suddenly, but rather had an intermittent onset, in a transition back and forth between filaments and void, so that the two modes alternated in time. This intermittent transition stage ended at approximately 160 s when there was only a single void.

The movement of the great void mode was a rotation in the horizontal plane, i.e., azimuthally. Some viewers have likened the rotating beam in the glow to a searchlight or light house beacon, turning around and around. Sample video data can be downloaded from Ref. [64]. The direction of rotation sometimes changed spontaneously in the middle of the cycle, although it usually turned the same direction. In a test, we shut off the gas flow, and the void still rotated. This indicates that the fundamental cause of the rotation is not gas flow, but some other effect. Phenomenologically, we can say that the great void moves something like a very slow striation in the glow. Fundamentally, however, we cannot explain the motion.

The great void had a distinct and sharp boundary. In the LLS images, there appears to be an abrupt jump in the dust number density, from zero inside the void to a finite value in the surrounding dusty plasma. The sharpness of the void edge is also seen in the time series for the floating potential (inset on the right side of Fig. 7) as the void rotated past the stationary probe.

During the great void mode, the particles resumed growing in diameter. This can be seen in Fig. 4, beginning at approximately 160 s. The number density in the interelectrode region also resumed its decline during the great void mode activity. (These number density measurements were made by optical extinction of a laser beam that passed in the lower portion of the dust cloud, where the void never reached.) In our visual observations of the LLS, we saw that during the great void mode activity, particles were expelled radially from the interelectrode region into the cold dark plasma that filled the rest of the vacuum vessel. Presumably this radial loss accounts for much, if not all, of the decline in the dust number density in the interelectrode region, as shown in Fig. 4.

Inside the great void, the glow was greatly enhanced, as can be seen in Figs. 5(c) and 6(c), and in the oblique horizontal view of Fig. 9. (In viewing these figures, recall that features in the glow always appear diffuse, because they are volume images, rather than images of a sharp cross section as in the case of the laser-illuminated dust.) Our synchronized video cameras showed that the reduction in dust number density in the void exactly coincides with an enhanced glow, just as it does in the filamentary mode.

Line-ratio imaging revealed that the energetic tail of the electron distribution is colder in the void than in the surrounding dusty plasma. This is shown in Fig. 10. This image indicates that the enhanced glow observed in the void must be due to electrons that are more dense, rather than hotter. This is consistent with Boeuf's prediction, based on particle-in-cell simulations [65], that sustaining a discharge when electrons are depleted by dust particles requires an increased electric field and a commensurate increase in the electron temperature. In our experiment, the electron temperature is higher and electrons are less dense in the dust cloud com-

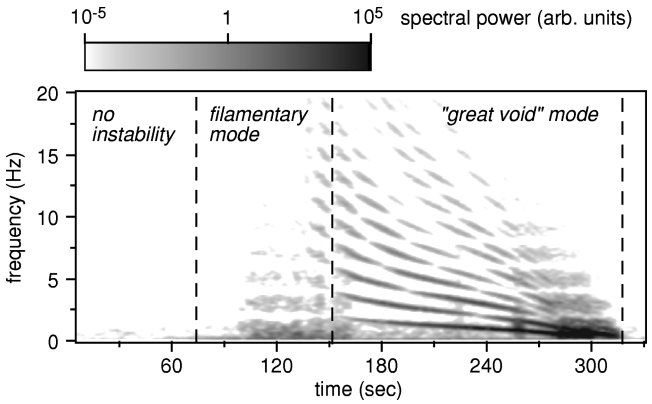

FIG. 11. Spectral power of dust number density fluctuations vs time. The gray scale is logarithmic, to allow easier identification of harmonics. The rotation speed of the great void mode diminishes with time. Harmonics in the great void mode are attributable to its nonlinearity (the dust density alternates between finite in the cloud and zero in the void.) The filamentary mode is better seen in Fig. 8, since its spectrum is peaked at frequencies higher than shown here.

pared to the pristine plasma of the void, due to electron depletion in a dusty plasma.

The particle charge and electron depletion in the dust cloud can be estimated from our measurements. Using orbital-motion limited theory [16] to compute the charge of an isolated particle of diameter 130 nm in a pristine plasma yields $Q/e=-244$ for $T_e=3$ eV. Using the measured values of n_e in a pristine plasma and the number density of particles n_d in the dust cloud, we found $P\approx 1-2$. Here P is the ''Havnes parameter'' which is roughly the ratio of the charge densities of dust particles and electrons [16,66]. Taking this into account, the charge on the grain is reduced by a factor of 0.2 or 0.6, depending on whether one assumes an ion density that is the same in the dust cloud and the pristine plasma, or a Boltzmann ion response, respectively. This represents a significant level of electron depletion.

The dust plasma frequency f_{pd} can also be estimated. This is a characteristic upper limit for compressional oscillations of the dust cloud. Computing $2\pi f_{\mathrm{pd}}=(Q^2 n_d/\epsilon_0 m_d)^{1/2}$, for 130-nm-diameter carbon particles with $Q=-244e$ and $n_d=10^8$ cm^{-3}, we find $f_{\mathrm{pd}}=14$ kHz. This value should be reduced by a factor of 0.2 or 0.6 to account for charge reduction due to electron depletion, yielding an f_{pd} of a few kHz.

The electric field in the void can be estimated from the floating potential measurements of Fig. 7. The floating potential is about 10 V more positive in the clean plasma of the void than in the dust cloud. Although we did not measure the plasma potential, it is reasonable to estimate that it varied by a similar amount. The half-width of the great void is approximately 0.5 cm. Therefore, we can estimate, to an accuracy better than an order of magnitude, that the electric field is 20 V/cm.

The rotation rate of the great void gradually diminished with time (and particle diameter). This can be seen in the spectrogram, Fig. 11. The gray scale in this figure represents spectral power of the dust number density fluctuations, as measured by single-point LLS. As the modes sweep around in space, the void repeatedly passed the detection point. We have plotted this spectrum with a logarithmic gray scale, to make the harmonics more easily seen. The harmonics are attributable to the nonlinearity of the mode, which appear to be almost like a square wave in Fig. 7.

Gas flow influenced the rotation of the void slightly, but it does not account for the rotation, or the instability for that matter. We observed the great void mode whether or not there was gas flow in the chamber. In the absence of gas flow the void rotated 360° with constant angular velocity, while in the presence of a moderate gas flow of 60 sccm the void slowed slightly while passing the gas inlet and occasionally reversed direction. When the void stopped rotating, it usually pointed toward the gas inlet, in cases when there was gas flow.

As the cycle progressed, the great void continued to grow in size. As it grew, it pushed further inward toward the center of the plasma. By the time it reached the center, it stopped rotating entirely. In Figs. 5(d) and 6(d), the void fills nearly half the central interelectrode volume. At this point the void stopped rotating. The slowing and stopping of the void can be seen in the floating potential time series in the right-hand inset of Fig. 7. (The time scale in Fig. 7 is somewhat slower than in all the other data presented here, due to slightly different discharge conditions.) After stopping, the great void continued to swell in size, pushing dust out of the interelectrode region.

As a test, we found that the development of the cycle at this point could be reversed by reducing the rf power. Recall that the rf power controls the ionization rate, and therefore the ion flux that drives the ion-drag force. After the dust cloud collapsed, reducing the rf power caused the dust cloud to raise and to fill more of the interelectrode region. The void became smaller, as it had been a minute or so earlier, and resumed rotating. This indicates the importance of ion drag for the void's existence.

Ultimately, the stationary void stopped, filling most of the interelectrode volume, and a fresh cloud of dust began growing inside it. In this way, the cycle renewed itself, and repeated over and over.

The physics conclusions we will incorporate in our phenomenological model of the instability, based on our observations of the great void mode, include the following: (1) Electrons are depleted in the dust cloud. (2) Ionization is enhanced in the void. (3) Ion drag is partly responsible for the void.

F. Growth rate using different materials

Experiments repeated with different electrode materials showed the same instability pattern for the dust particles grown from different materials, but the timing was different. Results are shown in Table I. The different time scales are attributable mainly to the different sputtering yields. This is because the particles grow from the flux of sputtered atoms. Aluminum was an outlier in this trend, which we attribute to the increased plasma exposure time required to clean the aluminum oxide film before the actual aluminum sputtering began.

Significantly, the particle diameter was always the same at the end of the instability cycle. This is true for all the materials that grew spherical particles, as listed in the final column of Table I. The measurements of particle diameter were made from SEM micrographs at the end of the cycle.

TABLE I. Timing of the instability, with dust grown from different materials. Times are indicated in hours (h), minutes (’), and seconds (’’) after the discharge was ignited. The sputtering yields are based on Ref. [72]. Particle diameters were measured by SEM at the end of the cycle, when the void stopped moving. Note that the particle size at the end of the cycle is exactly the same, regardless of the growth rate, and that the growth rate corresponds roughly to the sputtering yield. Epoxy sputtering produced a measurable dust cloud, but we were unable to image its particles afterwards using SEM.

Electrode material	Detectable dust	Onset of instability	Great void mode	Void stops	Sputtering yield (at 300 eV)	Particle diameter (nm)
Copper	15’’	2’ 30’’	4’	5’	1.59	fractal
Epoxy	20’’	1’ 30’’	2’ 30’’	3’	n/a	n/a
Graphite	30’’	1’ 15’’	2’ 40’’	4’ 20’’	0.1 (at 400 eV)	343 ± 11
Titanium	2’	4’ 30’’	23’	3 h	0.33	360 ± 65 S
Stainless steel	5’	9’	13’	1 h 24’	0.76 (for Fe)	350 ± 70
Tungsten	7’	16’	18’	2 h	0.4	360 ± 50
Aluminum	10’	15’ 30’’	17’	50’	0.65	fractal

Since the particle diameter was the same at the end of the cycle in each case, it is likely that it was the same earlier in the cycle as well, when the modes began. This offers support to the idea that the instabilities arise when the particle diameter exceeds a certain threshold.

Fractal-shaped particles grew when copper and aluminum targets were sputtered. These were different from the mainly spherical particles grown by sputtering the other materials we tested: graphite, titanium, stainless steel, and tungsten. For those materials, the particles formed mostly spheres, which appeared either solitary or in a coagulatant of only two or three spheres joined together. The physics conclusion from these tests that we will incorporate into our phenomenological model of the instability is that the time scale for the cycle, and therefore the onset of the instabilities, is controlled by the particle size.

V. DISCUSSION

A. The nature of the instability

Here we summarize some of the key observations of Sec. IV: (i) In the dust cloud, the electrons are depleted. (ii) The instabilities have an onset at a specific particle size. (iii) Ion drag is involved in the instability formation. (iv) The glow is modulated, indicating that ionization is enhanced in the glow. (v) The dust number density is also modulated, indicating that low-frequency electric fields are present. (vi) The void and glow are in phase, i.e., a reduction in the dust coincides with an augmented glow, indicating an enhanced ionization rate in the low-dust-density region. (vii) The enhanced ionization rate is attributable to a higher electron density, rather than to a higher T_e, which is consistent with electron depletion in the dust cloud.

The filamentary and great void modes have much in common, and they might indeed be different stages of the same instability. The distinction we make between them is essentially phenomenological. The filamentary mode appears first, with a sudden onset. It consists of numerous striations which move about with a characteristic frequency, as seen by a stationary detector, of about 100 Hz. The great void mode differs in that it is singular, slower, larger, and so highly nonlinear that the dust density is apparently zero inside the void. In both modes, the dust number density and glow are modulated, and are out of phase with one another.

To develop an explanation for the modes, it will later be important to recall that in a region of enhanced glow, the ionization and the outward ion flow will be correspondingly enhanced. This ion flow will apply an ‘‘ion drag force’’ to the particles. We discuss this and other forces next.

B. Forces acting on a particle

Dust particles are subject to electrical, mechanical, and optical forces in plasma. The electrical forces all depend on the particle charge Q, which is given by

$$Q/e = K_Q r k_B T_e, \tag{2}$$

where K_Q is a constant that must be calculated numerically, r is the particle radius, and T_e is the electron temperature [16]. Note the scaling $Q \propto r$.

The electrostatic force is

$$F_{\mathrm{el}} = QE,$$

where E is the electric field. Note that

$$F_{\mathrm{el}} \propto r.$$

The ion drag force consists of two components: the orbit and collection forces [67]. The latter is negligible for 100-nm particles, provided that the ion drift velocity v_i satisfies $v_i < 3000$ m/s and $E < 70$ kV/m, which are the case for our plasma. The orbit force, due to the Coulomb deflection of ions moving at velocity v_i past a charged grain, is [67]

$$F_{\mathrm{io}} = n_i v_s m_i v_i 4\pi b_{\pi/2}^2 \Lambda,$$

where n_i, m_i, and T_i are the ion density, mass, and temperature, respectively,

$$v_s = \sqrt{\frac{8k_B T_i}{\pi m_i} + v_i^2}$$

is the average ion speed, k_B is the Boltzmann constant,

$$b_{\pi/2} = qQ/4\pi\epsilon_o m_i v_s^2$$

is the impact parameter whose asymptotic orbit angle is $\pi/2$, ϵ_o is the vacuum permittivity, and Λ is the Coulomb logarithm [68], where we use the modified form of Barnes *et al.* [67] for a charged sphere of finite radius. Note that the ion drag force scales as

$$F_{\mathrm{io}} \propto r^2.$$

In its velocity dependence, it is peaked near the ion thermal velocity, at $v_i = 1.129\sqrt{k_B T_i / m_i}$.

In computing the ion drag force, the ion drift velocity v_i can be assumed to be mobility limited,

$$v_i = \mu E / p,$$

where p is the gas pressure and the mobility μ is velocity dependent. It has been found empirically [69] that

$$\mu = \frac{\mu_o}{\sqrt{1 + aE/p}},$$

where the coefficients μ_o and a depend on the gas, and are tabulated in Ref. [69].

Note that both the electric and ion drag forces are driven by the electric field, but in opposite directions. When the particles are negatively charged, as in most gas discharges, these two forces will point in opposite directions. Due to the negative charge, F_{el} will point opposite to E, whereas the ion flow direction and therefore F_{io} will be in the same direction as E.

The forces scale differently with particle size, $F_{\mathrm{el}} \propto r$ and $F_{\mathrm{io}} \propto r^2$. The electric force will thus dominate for small particles, while ion drag will dominate for larger particles. In our experiment, as the particle size grows, there is a critical moment when the ion drag force exceeds the electrostatic force, rather than the other way around. The net force on a particle suddenly reverses direction as the particle size grows. It is not hard to imagine that this might produce an instability with a sudden onset, and that is what we will propose below.

There are several other forces that also act on the particles. In our experiment the only one of significance is neutral gas drag, which is $\propto r^2$. It surely dissipates energy from the modes, since the dust moves against this force when it is accelerated by the electric fields of the modes. All other forces are assumed to be negligible. Both electrodes were water cooled to avoid thermophoresis, which scales $\propto r^2$, and can be significant when there is a substantial temperature gradient in the plasma, as shown in Ref. [70]. The Lorentz, polarization, and optical pressure forces were insignificant in our experiment. Gravity, which is $\propto r^3$, is small compared to the electrostatic and ion drag forces, due to the small particle size in our experiment.

C. Empirical model of the instability mechanism

The following empirical model of the instabilities is supported by all the experimental evidence we have presented. Suppose that in a uniform dust cloud in a gas discharge, there is a spontaneous fluctuation in the dust number density. In the region of reduced dust density, there will be less depletion of the electrons by the dust. This will lead to a higher electron density there, and a correspondingly higher ionization rate. This ionization hot spot will develop a positive space charge with respect to the surrounding medium. The resulting outward electric field will apply two forces to the negatively charged dust particles: an inward electrostatic force and an outward ion drag force. For a small particle size, the inward force will dominate, and the hot spot will be filled up once again by dust, and the fluctuation will disappear. This is the initial stable equilibrium. As the particle size grows, it reaches a critical level, where the outward ion drag force exceeds the electrostatic force. The region of reduced dust density will then expel more of its dust particles, and the fluctuation will grow. This is an instability. The threshold for the instability is determined by particle size and electric field strength. The particle size is an independent parameter, whereas the electric field is determined self-consistently by the transport mechanisms in the glow discharge. Near the critical point, a small change in the particle size leads to a sudden onset of an instability.

D. Critical condition for sustaining the void

To verify quantitatively that the above empirical model of the instability is reasonable, here we calculate the critical size of the particle diameter for the void to persist. We computed the charge of an isolated particle using Eq. (2) and experimental parameters, and we halved this value to account for the effect of electron depletion. We assumed an electric field $E = 20$ V/cm, as determined from the probe measurements. Plotting the two forces as a function of particle diameter, we found that the curves for F_{el} and F_{io} crossed at a critical diameter of 160 nm. This result is consistent with the observed value of 120 nm at the transition to the great void mode.

The sources of error in this calculation include the particle charge and the value of the electric field. The latter was estimated as $E = \Delta\phi / l$, where $\Delta\phi$ is the variation of plasma potential, which was assumed to be equal to the variation of the floating potential, and l is the characteristic size of the void. Both of these values may have an error by a factor of 2. The calculation of the particle charge may be subject to a comparable uncertainty. Given the level of these errors, we find that our computed value of 160 nm is in good agreement with the measured value of 120 nm.

VI. CONCLUSION

Using a dust cloud in a glow discharge, we have characterized an instability. As particles grew in size, there was a sudden onset of an instability. As it developed, we observed first the filamentary mode and then the great void mode. The great void mode is characterized by a dust-free region that rotates around the vertical axis.

We found that inside a region of reduced dust density, there is an enhanced glow, indicating an enhanced ionization. This ionization hot spot is due to a higher electron density, commensurate with a reduction in electron depletion when the dust is more sparse. The modes have a sufficiently low frequency that the electric field can move the dust particles about.

The following empirical model of the instabilities is consistent with the observations. In a region of reduced dust

density, a reduced depletion of the electrons by the dust leads to a higher electron density and a correspondingly higher ionization rate. This hot spot in the ionization develops a positive space charge with respect to the surrounding medium. The resulting electric field points outward from the center of the hot spot, and applies two forces to the negatively charged dust particles. The electrostatic force is inward and ion drag force is outward. These two forces scale linearly and with the square of the particle size, respectively. As the particle size increases, it reaches a critical level where the outward ion drag force exceeds the electrostatic force. This causes the instability. The critical particle size depends on the electric field strength, which is determined self-consistently by the glow-discharge transport mechanisms.

We believe that our phenomenological explanation of the instability is well supported by the experiment. Nevertheless, we have not developed this model into a complete quantitative theory. To do so would require, first of all, a linear dispersion relation that could be used to predict the imaginary part of the frequency, and thereby predict the onset of the instability. This must include the ion drag force, which does not appear in existing theoretical dispersion relations [43,44], and a self-consistent electric field for the actual gas discharge transport conditions. Second, it would require a nonlinear model to explain the actual experimental observations, such as the void's size and its sharp boundary. In the experiment, a linear stage of exponential growth was never observed. Rather, we observed the sudden onset of an instability to a fully saturated nonlinear state.

Such a theoretical model, if it is extremely successful, might explain aspects of our experiment that we cannot explain based on our empirical model. These unexplained observations include the physical location of the void (off center in the plasma) and its rotation.

In the experiment, we also characterized dust particle growth in the gas phase, due to sputtering. The growth history is similar to that of silane deposition discharges, but at a slower time scale. Initially the particle growth rate is high, and the particle number density decreases rapidly, while later on the growth rate becomes lower and the number density is constant. This behavior is attributed to initial growth by coagulation and later growth by the film deposition on the particle surface. Electron micrographs show the dust particles to be approximately spherical and monodisperse.

After submitting this paper the authors learned of a related paper by Melzer, Piel, and Schweigert [71], which presented the experiments on very low-frequency self-excited oscillations of dust-free regions in silane discharges and an analytical model based on dust growth dynamics explaining these oscillations. They observed a void similar to our great void, except that it did not rotate and it was located more centrally, unlike the radial-spoke shape of our great void. Also, D'Angelo produced a theoretical dispersion relation that includes the effects of ion drag, yielding an instability at a critical electric field, which is analogous to the critical particle size in our experiment [45].

ACKNOWLEDGMENTS

We thank N. D'Angelo, M. Malyshev, R. Merlino, V. Tsytovich, and S. Vladimirov for helpful discussions. This work was supported by NASA and the National Science Foundation. The authors thank G. Morfill for facilities at the Max Planck Institut.

[1] G. Selwyn, J. Singh, and R. Bennet, J. Vac. Sci. Technol. A **7**, 2758 (1989).
[2] L. Boufendi, J. Hermann, A. Bouchoule, B. Dubreuil, E. Stoffels, W. W. Stoffels, and M. L. de Giorgi, J. Appl. Phys. **76** (1), 148 (1994).
[3] K. Spears, T. Robinson, and R. Roth, IEEE Trans. Plasma Sci. **PS-14**, 179 (1986).
[4] G. Selwyn, J. McKillop, K. Haller, and J. Wu, J. Vac. Sci. Technol. A **8**, 1726 (1990).
[5] G. Jellum and D. Graves, J. Appl. Phys. **67**, 6490 (1990).
[6] S. Geha, R. Carlile, J. O'Hanlon, and G. Selwyn, J. Appl. Phys. **72**, 374 (1992).
[7] R. Buss and S. Babu, J. Vac. Sci. Technol. A **14**, 577 (1996).
[8] H. Hahn and R. Averback, J. Appl. Phys. **67**, 1113 (1990).
[9] G. Chow, R. L. Holtz, A. Pattnaik, A. S. Edelstein, T. E. Schlesinger, and R. C. Camarata, Appl. Phys. Lett. **56**, 1853 (1990).
[10] B. Draine and B. Sutin, Astrophys. J. **320**, 803 (1987).
[11] T. Northrop, Phys. Scr. **45**, 475 (1992).
[12] O. Havnes, T. Aslaksen, F. Melandsø, and T. Nitter, Phys. Scr. **45**, 491 (1992).
[13] T. Nitter and O. Havnes, Earth, Moon, Planets **56**, 7 (1992).
[14] G. Praburam and J. Goree, Astrophys. J. **441**, 830 (1995).
[15] J. Nuth and B. Donn, J. Chem. Phys. **77**, 2639 (1982).
[16] J. Goree, Plasma Sources Sci. Technol. **3**, 400 (1994).
[17] A. Barkan, R. Merlino, and N. D'Angelo, Phys. Plasmas **2**, 3563 (1995).
[18] J. Ma and M. Yu, Phys. Plasmas **1**, 3520 (1994).
[19] A. Barkan, N. D'Angelo, and R. Merlino, Planet. Space Sci. **44**, 239 (1996).
[20] M. Rosenberg, J. Vac. Sci. Technol. A **14**, 631 (1996).
[21] N. D'Angelo and R. Merlino, Planet. Space Sci. **44**, 1593 (1996).
[22] H. Ikezi, Phys. Fluids **29**, 1764 (1986).
[23] H. Thomas, G. E. Morfill, V. Demmel, J. Goree, B. Feuerbacher, and D. Möhlmann, Phys. Rev. Lett. **73**, 652 (1994).
[24] Y. Hayashi and K. Tachibana, Jpn. J. Appl. Phys. Part 1 **33**, L804 (1994).
[25] J. Chu and I. Lin, Physica A **205**, 183 (1994).
[26] J. Chu and I. Lin, Phys. Rev. Lett. **72**, 4009 (1994).
[27] A. Melzer, T. Trottenberg, and A. Piel, Phys. Lett. A **191**, 301 (1994).
[28] J. Pieper, J. Goree, and R. Quinn, J. Vac. Sci. Technol. A **14**, 519 (1996).
[29] G. Morfill and H. Thomas, J. Vac. Sci. Technol. A **14**, 490 (1996).
[30] K. Tachibana and Y. Hayashi, Aust. J. Phys. **48**, 469 (1995).
[31] J. Pieper and J. Goree, Phys. Rev. Lett. **77**, 3137 (1996).

[32] G. Praburam and J. Goree, Phys. Plasmas **3**, 1212 (1996).
[33] L. Boufendi and A. Bouchoule, Plasma Sources Sci. Technol. **3**, 262 (1994).
[34] C. Cui and J. Goree, IEEE Trans. Plasma Sci. **22**, 151 (1994).
[35] N. D'Angelo, Planet. Space Sci. **42**, 507 (1994).
[36] C. Li and M. Tsai, J. Mater. Sci. **28**, 4562 (1993).
[37] N. Rao, P. Shukla, and M. Yu, Planet. Space Sci. **38**, 543 (1990).
[38] D. Winske, S. Gary, and M. Jones, Geophys. Res. Lett. **22**, 2069 (1995).
[39] N. D'Angelo, Planet. Space Sci. **38**, 1143 (1992).
[40] F. Melandsø, T. Aslaksen, and O. Havnes, Planet. Space Sci. **41**, 321 (1993).
[41] M. Rosenberg, Planet. Space Sci. **41**, 229 (1993).
[42] C. Thompson, A. barkan, N. D'Angelo, and R. Merlino, Phys. Plasmas **4**, 2331 (1997).
[43] P. Shukla and G. Morfill, Phys. Lett. A **216**, 153 (1996).
[44] N. D'Angelo, Phys. Plasmas **4**, 3422 (1997).
[45] N. D'Angelo, Phys. Plasmas **5**, 3155 (1998).
[46] A. Garscadden, in *Gaseous Electronics*, edited by M. Hirsh and H. Oskam (Academic, New York, 1978), Vol. 1.
[47] D. Douglas-Hamilton and S. Mani, Appl. Phys. Lett. **23**, 508 (1973).
[48] E. Gogolides, M. Stathakopoulos, and A. Boudouvis, J. Phys. D **27**, 1878 (1994).
[49] G. Bohren and D. Huffman, *Absorption and Scattering of Light by Small Particles* (Wiley, New York, 1983).
[50] H. V. de Hulst, *Light Scattering by Small Particles* (Dover, New York, 1981).
[51] J. Hodkinson, J. Opt. Soc. Am. **54**, 846 (1964).
[52] A. Pluchino, S. Goldberg, J. Dowling, and C. Randall, Appl. Opt. **19**, 3370 (1980).
[53] M. Buie, J. Pender, J. Holloway, and M. Brake, IEEE Trans. Plasma Sci. **24**, 111 (1996).
[54] M. Buie, J. T. Pender, T. Vincent, J. P. Holloway, M. L. Brake, and M. Elta, Proc. SPIE **2091**, 211 (1994).
[55] W. Hareland and R. Buss, IEEE Trans. Plasma Sci. **24**, 117 (1996).
[56] R. McWhirter, in *Plasma Diagnostic Techniques*, edited by R. Huddlestone and S. Leonard (Academic, New York, 1965).
[57] H. Griem, *Plasma Spectroscopy* (McGraw-Hill, New York, 1964).
[58] R. Rhoades and S. Gorbatkin, J. Appl. Phys. **80**, 2605 (1994).
[59] T. Desai, S. V. Gogawale, A. B. Shukla, N. K. Joshi, U. S. Salgaonkar, and G. L. Bhale, Vacuum **46**, 223 (1995).
[60] K. Junck and W. Getty, J. Vac. Sci. Technol. A **12**, 2767 (1994).
[61] M. Malyshev and V. Donnelly, J. Vac. Sci. Technol. A **15**, 550 (1997).
[62] V. Godyak and R. Piejak, Phys. Rev. Lett. **65**, 996 (1990).
[63] V. Godyak, R. Piejak, and B. Alexandrovich, Plasma Sources Sci. Technol. **1**, 36 (1992).
[64] D. Samsonov and J. Goree, http://;dusty.physics.uiowa.edu/Movies/Movie-index.html.
[65] J. Boeuf, Phys. Rev. A **46**, 7910 (1992).
[66] O. Havnes, T. Aanesen, and F. Melandsø, J. Geophys. Res. **95**, 6581 (1990).
[67] M. Barnes, J. H. Keller, J. C. Forster, J. A. O'Neil, and D. K. Coultas, Phys. Rev. Lett. **68**, 313 (1992).
[68] J. Bittencourt, *Fundamentals of Plasma Physics* (Pergamon, New York, 1986).
[69] L. Frost, Phys. Rev. **105**, 354 (1957).
[70] G. Jellum, J. Daugherty, and D. Graves, J. Appl. Phys. **69**, 6923 (1991).
[71] A. Melzer, A. Piel, and V. Schwiegert (unpublished).
[72] N. Laegreid and G. Wehner, J. Appl. Phys. **32**, 365 (1961).